John von Neumann Institute for Computing


# The Korringa-Kohn-Rostoker (KKR) Green Function Method II. Impurities and Clusters in the Bulk and on Surfaces

Peter H. Dederichs, Samir Lounis, and Rudolf Zeller

published in

*Computational Nanoscience: Do It Yourself!*,
J. Grotendorst, S. Blügel, D. Marx (Eds.),
John von Neumann Institute for Computing, Jülich,
NIC Series, Vol. **31**, ISBN 3-00-017350-1, pp. 279-298, 2006.



http://www.fz-juelich.de/nic-series/volume31

# The Korringa-Kohn-Rostoker (KKR) Green Function Method II. Impurities and Clusters in the Bulk and on Surfaces

**Peter H. Dederichs, Samir Lounis, and Rudolf Zeller**

Institute for Solid State Research
Forschungszentrum Jülich
52425 Jülich, Germany
*E-mail: {p.h.dederichs, s.lounis, ru.zeller} @fz-juelich.de*

## 1 Green Function Method

In density functional calculations the solution of the Kohn-Sham equations for the single-particle wave functions $\varphi_\alpha(\mathbf{r})$ and the corresponding eigenvalues $\varepsilon_\alpha$, the single-particle energies, represents the central problem. Thus most of electronic structure calculations follow this route, i.e. calculating eigenfunctions $\varphi_\alpha$ and eigenvalues $\varepsilon_\alpha$. However, the calculation of $\varphi_\alpha$ and $\varepsilon_\alpha$ can be avoided, if instead the single-particle Green function $G(\mathbf{r}, \mathbf{r}'; E)$ of the Kohn-Sham equation is determined, since this quantity contains all the information about the ground state. In particular the charge density and the local density of states can be directly calculated from the Green function, which is the solution of the Schrödinger equation for an energy $E$ with a source at position $\mathbf{r}'$:

$$(-\partial_r^2 + V(\mathbf{r}) - E)\, G(\mathbf{r}, \mathbf{r}'; E) = -\delta(\mathbf{r} - \mathbf{r}') \quad , \tag{1}$$

with atomic units $\hbar^2/2m = 1$ used. Using the spectral representation for the (retarded) Green function

$$G(\mathbf{r}, \mathbf{r}'; E + i\epsilon) = \sum_\alpha \frac{\psi_\alpha(\mathbf{r})\psi_\alpha^*(\mathbf{r}')}{E + i\epsilon - E_\alpha} \quad . \tag{2}$$

it is easy to show that the charge density $n(\mathbf{r})$ can be directly expressed by an energy integral over the imaginary part of the Green function:

$$n(\mathbf{r}) = 2 \sum_{\substack{\alpha \\ E_\alpha < E_F}} |\psi_\alpha(\mathbf{r})|^2 = -\frac{2}{\pi} \int^{E_F} dE\, \mathrm{Im}\, G(\mathbf{r}, \mathbf{r}; E) \tag{3}$$

This relation directly allows calculation of the charge density from the imaginary part of the Green function, which can be interpreted as the local density of states at the position $\mathbf{r}$. The local density of states of a particular atom in a volume $V$ is obtained by integrating over this volume

$$n_V(E) = -\frac{2}{\pi} \int_V d\mathbf{r}\, \mathrm{Im}\, G(\mathbf{r}, \mathbf{r}; E) \quad . \tag{4}$$

In this way the evaluation of the wave-functions $\psi_\alpha(\mathbf{r})$ can be avoided. Due to the strong energy-dependent structure of the density of states, the evaluation of the energy integral is

usually very cumbersome and typically about $10^3$ energy points are needed in an accurate evaluation of this integral.

The numerical effort can be strongly decreased, if the analytical properties of the Green function $G(z)$ for complex energies $z = E + i\Gamma$ are used. Since $G(z)$ is analytical in the whole complex energy plane, the energy integral can be transformed into a contour integral in the complex energy plane

$$n(\mathbf{r}) \;=\; -\frac{2}{\pi}\,\mathrm{Im}\int_{E_B}^{E_F} dz\, G(\mathbf{r},\mathbf{r};z) \tag{5}$$

where the contour starts at an energy $E_B$ below the bottom of the valence bands, goes into the complex plane and comes back to the real axis at the Fermi level. Since for complex energies all structures of the Green function are broadened by the imaginary part $\Gamma$, the contour integral can be accurately evaluated using rather few energy points, typically 20-30, leading to a large saving of computer time. In this way Green function methods are competitive to diagonalization methods. Additional advantages occur for systems with two- or three-dimensional symmetry, since as a result of the energy broadening the $\mathbf{k}$–integration over the Brillouin zone for complex energies requires much less $\mathbf{k}$–points. In the evaluation of the contour integral, special care is necessary for the piece of the path close to $E_F$, since here the full structure of $G(E)$ on the real axis reappears. Therefore the energy mesh should become increasingly denser when approaching $E_F$.

The integration over a complex energy contour can also be extended to finite temperatures by using the analytical properties of the Fermi-Dirac distribution. Here the essential point is that the contour close to $E_F$ is replaced by a sum over Matsubara energies $z_j = E_F + i\pi(2j-1)kT$, $j = 1, 2, \ldots$. Then only complex energies are needed, since the energy point closest to $E_F$ has still an imaginary part of $\pi kT$. This is of particular advantage, when a discrete $k$-mesh is used, like e.g. in the special points method.

The real problem is the evaluation of the Green function for the system of interest. For this one does not go back to Eq. (2), since this would mean the evaluation of all eigenvalues $\varepsilon_\alpha$ and wave functions $\varphi_\alpha$, which one wants to avoid. Rather one relates the Green function $G$

$$G(E) = \frac{1}{E + i\varepsilon - H} \;=\; \frac{1}{E + i\varepsilon - H_o - V} \tag{6}$$

of a system with Hamiltonian $H = H_o + V$ to the Green function $G_o = \{E + i\varepsilon - H_o\}^{-1}$ of a reference system, which is analytically known or easy to calculate. Then $G(E)$ can be obtained from the Dyson equation

$$G(E) = G_o(E) + G_o(E)\, V\, G(E) = G_o\, \frac{1}{1 - VG_o} \quad . \tag{7}$$

For instance, for a bulk crystal one starts with the free space Green function $G_o(H_o = -\partial_{\mathbf{r}}^2)$, such that $V$ is the sum of the potentials of all atoms (for details see the lecture of Mavropoulos et Papanikolaou on page 131). For the surface Green function $G_o$ is identified with the bulk Green function, such that $V$ is the difference between the potentials at the surface and in the bulk. Analogously for an impurity in a crystal one starts again with the bulk Green function $G_o$, such that $V$ represents the change of the impurity potential with respect to the bulk potential as well as the perturbation of the potentials of the neighboring host atoms. Most important is, that the perturbed potential $V$ is well localized near the

impurity, while the perturbed wave functions are not localized and accurately described by the Dyson equation.

Such impurity problems are often described by an 'Ersatzgeometry', e.g. an impurity in a relatively small cluster of bulk atoms or by a supercell geometry with a periodic array of impurities. In these cases the boundary conditions for the wave functions are changed violently, since e.g. for a cluster all wave functions are restricted to the size of the cluster. Therefore the introduction of the host Green function $G_o$ solves the socalled "embedding problem", since it correctly describes the embedding of the impurity in the infinite bulk system. Needless to say, that the Green function method can not only be applied to a single impurity, but also to a small cluster of impurity atoms in the bulk, provided that the perturbation of the potential is localized in a restricted area. Moreover, once the Green function of the surface is known, one can calculate the electronic structure of an impurity or of small clusters at surfaces with an analogous Dyson equation.

## 2 KKR Green Function Method for Impurities

In the method of Korringa, Kohn and Rostoker (KKR)[1] the Schrödinger equation is solved by multiple scattering theory, describing the propagation of a wave in the solid as a repetition of single scattering events at the different atoms. Thus first the single scattering event of the wave at the potential of the different single atoms $n$ is calculated, described by the single site "t-matrix" $t_{n'}$, and then the multiple scattering at the given arrangement of the atoms in the crystal. The resulting equations show a beautiful separation between potential and structural properties, which are typical for the KKR method. In the following we summarize here the most important results; for more details, we refer to Ref. 2 and the lecture of Ph. Mavropoulos in this school.

In the KKR Green function method one divides the whole space into non–overlapping and space–filling cells centered at positions $\mathbf{R}^n$. In each cell the electrons are scattered by potentials $v^n$, which in this section are assumed to be spherically symmetric and centered at $\mathbf{R}^n$. By introducing cell-centered coordinates the Green function $G(\mathbf{r}+\mathbf{R}^n, \mathbf{r}'+\mathbf{R}^{n'}; E)$ can then be expanded in each cell as a function of $\mathbf{r}$ and $\mathbf{r}'$ into spherical harmonics:

$$G(\mathbf{r}+\mathbf{R}^n, \mathbf{r}'+\mathbf{R}^{n'}; E) = \delta_{nn'}\sqrt{E}\sum_L H_L^n(\mathbf{r}_>; E) R_L^n(\mathbf{r}_<; E) + \sum_{LL'} R_L^n(\mathbf{r}; E)\, G_{LL'}^{nn'}(E)\, R_{L'}^{n'}(\mathbf{r}; E) \quad . \tag{8}$$

Here $\mathbf{r}$ and $\mathbf{r}'$ are restricted to the cells $n$ and $n'$ and $\mathbf{r}_<$ and $\mathbf{r}_>$ denote the one of the two vectors $\mathbf{r}$ and $\mathbf{r}'$ which has the smaller or larger absolute value. The $R_L^n(\mathbf{r}; E)$ and $H_L^n(\mathbf{r}; E)$ are the product of spherical harmonics and radial eigenfunctions to the central potential $v^n(r)$:

$$R_L^n(\mathbf{r}; E) = R_l^n(r; E)\, Y_L(\mathbf{r}) \tag{9}$$

$$H_L^n(\mathbf{r}; E) = H_l^n(r; E)\, Y_L(\mathbf{r}). \tag{10}$$

Here $R_L^n(\mathbf{r}, E)$ is the regular solution which varies at the origin as $r^l$ and which represents the solution for an incoming spherical Bessel function $j_l(\sqrt{E}r)Y_L(\mathbf{r})$, while $H_l^n$ is the corresponding irregular solution varying as $1/r^{l+1}$ at the origin and being identical

with the spherical Hankel function $h_l(\sqrt{E}r)$ outside the range of the potential. Both radial functions are connected by the Wronskian relation, which guarantees that the first term in Eq. (8) represents the exact Green function for the single potential $v^n(r)$ in free space. Since this term satisfies already the source condition $-\delta(\mathbf{r}-\mathbf{r}')$ for the Green function of Eq. (1), the second term is source free and contains in the double angular momentum expansion only the regular solutions $R^n_L$ and $R^{n'}_{L'}$.

By construction, the expression in Eq. (8) for the Green function satisfies in each cell $n$ the general solution of the Schrödinger equation (1) for the Green function, while the matrix $G^{nn'}_{LL'}(E)$, the so-called *structural Green function*, describes the connection of the solutions in the different cells and thus contains all the information about the multiple scattering problem, which is in this way reduced to the solution of an algebraic problem. The clear separation between the single–site properties, described by the radial solutions $R^n_L(\mathbf{r})$ and $H^n_L(\mathbf{r})$ and the multiple scattering properties as described by the matrix $G^{nn'}_{LL'}$, is the main advantage of the KKR method.

In principle, the structural Green function matrix $G^{nn'}_{LL'}(E)$ can be determined by matching the solutions of the neighboring cells at the cell boundaries. However at the cell boundaries the angular momentum expansion converges rather slowly, so that presumably a large $l_{\max}$ cut-off would be needed. The more elegant and at the same time more efficient way consists in using the power of multiple scattering theory, where the Green function is basically only needed in the inner region of the cell, where the potential is strong, so that the $l$–convergence represents no problem. As shown by Beeby and others[1], the structural Green function matrix can be determined from the corresponding matrix $g$ in free space by the Dyson equation

$$G^{nn'}_{LL'}(E) = g^{nn'}_{LL'}(E) + \sum_{n''L''} g^{nn''}_{LL''}(E)\; t^{n''}_{l''}(E)\; G^{n''n'}_{L''L'}(E) \tag{11}$$

where the $t$-matrix $t^n_l$ for the potential $v^n(r)$ is given by

$$t^n_l(E) = \int_0^R r^2\, dr\; j_l(\sqrt{E}r)\; v^n(r)\; R^n_l(r;E) \tag{12}$$

The derivation of this equation is lengthy and straightforward, so that we refer for this to the literature cited above. An elementary derivation, valid also for the full–potential case, has been given by Zeller[3].

Once the structural Green function $\mathring{G}^{nn'}_{LL'}(E)$ of the ideal crystal is known, the Green function $G^{nn'}_{LL'}(E)$ for the crystal with impurity can be evaluated by a modified Dyson equation

$$G^{nn'}_{LL'} = \mathring{G}^{nn'}_{LL'} + \sum_{n''L''} \mathring{G}^{nn''}_{LL''}\; \Delta t^{n''}_{l''}\; G^{n''n'}_{L''L'} \quad , \quad \Delta t^n_l = t^n_l - \mathring{t}^n_l \tag{13}$$

where $\Delta t^n_l$ is the difference $t^n_l - \mathring{t}^n_l$ between the $t$-matrices in the perturbed and in the ideal lattice. Since this difference, determined by the perturbation of the potential, is restricted to the vicinity of the impurity, the Green function in this subspace can be easily determined in real space by matrix inversion. The rank of the matrices to be inverted is given by $(l_{\max}+1)^2 \cdot n_d$, i.e. the number $n_d$ of perturbed potentials times the number $(l_{\max}+1)^2$ of angular momenta used. Here $l_{\max}$ is the maximum angular momentum used in the calculations, e.g. $l_{\max} = 3$.

For a single impurity it is often sufficient to neglect the perturbation of the neighboring host atoms and to take into account in Eq. (13) only the perturbation due to the impurity potential into account. This so-called single site approximation gives a quite reasonable description of the electronic structure of the impurity and is the essential ingredient of the coherent potential approximation for random alloys. For a more accurate description the perturbations of the neighbors have to be included. The size of the perturbation naturally increases, if impurity pairs, trimers or larger clusters of impurities are included. As a rule one should not only take the strong scattering centers into account, but also the perturbations of all first neighbor atoms.

If we consider an impurity or an adatom on a surface, the structure of the Dyson equation (13) is the same. One has only to replace the host Green function $\overset{\circ}{G}{}^{nn'}_{LL'}$ by the Green function of the ideal (unperturbed) surface and has to identify $\Delta t^n_l$ by the change of the $t$-matrix on site $n$ with respect to the value of the unperturbed surface. Thus it is the structural Green function $\overset{\circ}{G}{}^{nn'}_{LL'}$, which describes the correct embedding in the local environment. Therefore the calculation of $\overset{\circ}{G}{}^{nn'}_{LL'}$ represents the high entrance fee one has to pay in Green function calculations.

## 3 Full-Potentials, Forces and Lattice Relaxations

All-electron methods based on a spherical potential of muffin-tin type or on the atomic sphere approximation (ASA) have in general proven to be very successful and efficient for the description of the electronic structure of solids. However systems with lower symmetry and/or open structures require a more accurate treatment going beyond the spherical approximation. In particular this is necessary, if forces and lattice relaxations are calculated, since for these problems the spherical approximation fails completely.

The fundamental equation (8) for the KKR Green function is also valid in the full-potential case, so that the important separation between the single-potential problem and the multiple-scattering problem fully survives. However the single-site eigenfunctions $R^n_L(\mathbf{r};E)$ and $H^n_L(\mathbf{r};E)$ are now the solutions for the general potential $v^n(\mathbf{r})$ being no longer spherical[3]. For instance, $R^n_{L'}(\mathbf{r};E)$ is the solution of the Schrödinger equation for a spherical wave $j_{l'}(\sqrt{E}r)Y_{L'}(\mathbf{r})$ incident on the potential $v(\mathbf{r})$

$$R_{L'}(\mathbf{r};E) = j_{l'}(\sqrt{E}r)Y_{L'}(\mathbf{r}) + \int d^3r' g(\mathbf{r},\mathbf{r}';E)v(\mathbf{r}')R_{L'}(\mathbf{r}';E) \tag{14}$$

where $g(\mathbf{r},\mathbf{r}';E)$ is the Green function for free space. Clearly the index $L'$ refers to the angular momentum of the incoming partial wave. Solving Eq. (14) in this form would require a three dimensional integration. By expanding both the potential as well as the wave function $R_{L'}(\mathbf{r};E)$ into spherical harmonics:

$$v(\mathbf{r}) = \sum_L v_L(r)Y_L(\mathbf{r}) \tag{15}$$

$$R_{L'}(\mathbf{r};E) = \sum_L R_{LL'}(r)Y_L(\mathbf{r}) \tag{16}$$

we obtain coupled radial equations for the double indexed radial functions $R_{LL'}$

$$R_{LL'}(r;E) = \delta_{LL'} j_{l'}(\sqrt{E}r) + \int_0^S dr' r'^2 g_l(r,r';E) \sum_{L''} v_{LL''}(r) R_{L''L'}(r';E). \quad (17)$$

Here the first index $L$ refers to the **r**-coordinate of the outgoing partial wave and the second one $L'$ to the angular momentum of the incoming wave. The radial integral extends up to the range $S$ of the potential. Moreover

$$v_{LL'}(r) = \sum_{L''} C_{LL'L''} v_{L''}(r) \quad (18)$$

where $C_{LL'L''} = \int d\Omega Y_L Y_{L'} Y_{L''}$ are the Gaunt coefficients.

The solution of the integral equation (17) or of the equivalent differential equation is rather complicated[4]. In order to avoid numerical problems one transforms Eq. (17) into a modified integral equation[4], where the effect of the spherical part of the potential is already included in the incident radial wave function $\overset{\circ}{R}_l\ (r;E)$

$$\begin{aligned} R_{LL'}(r;E) &= \delta_{LL'}\ \overset{\circ}{R}_l\ (r;E) \\ &+ \int_0^S dr' r'^2 G_l(r,r';E) \sum_{L''} \Delta v_{LL''}(r) R_{L''L'}(r';E) \end{aligned} \quad (19)$$

and where $G_l(r,r';E)$ is the $l$-dependent radial Green function for the spherical component of the potential

$$G_l(r,r';E) = \sqrt{E}\ \overset{\circ}{H}_l\ (r_>;E)\ \overset{\circ}{R}_l\ (r_<;E) \quad (20)$$

and $\Delta v_{LL'}$ the non-spherical component of the potential

$$\Delta v_{LL'}(r) = \sum_{L''\neq 0} C_{LL'L''} v_{L''}(r) \quad (21)$$

which provides the coupling between the different angular momenta. Since the non-spherical potential $\Delta v$ is always rather small, we solve Eq. (19) by iteration, being equivalent to a Born series expansion in powers of $\Delta v$. Usually 2-4 iterations are sufficient for convergence.

While for non-spherical potentials the general Eq. (8) for the Green function remains valid and only $R_L(\mathbf{r})$ and $H_L(\mathbf{r})$ have to be replaced by the single-site solutions for the anisotropic potential, the same is also true for the Dyson equations (11) and (13) describing the multiple scattering. Only the t-matrix $t_l^n(E)$ has to be replaced by the t-matrix $t_{LL'}^n(E)$ for a general potential $v^n(\mathbf{r})$ being given by

$$t_{LL'}^n(E) = \int_0^S dr' r'^2 j_l(\sqrt{E}r') \sum_{L''} v_{LL''}^n(r') R_{L''L'}^n(r';E) \quad (22)$$

Since the Green functions occurring in the Dyson equation are anyhow $L,L'$-matrices, the numerical effort in solving the multiple scattering problem is the same for both spherical and non-spherical potentials. Therefore the additional numerical effort for full potentials scales in the KKR method only linearly with the number $N$ of non-equivalent atoms,

meaning that in typical calculations the full-potential method does not require a significant increase in computing time.

In case of a full-potential treatment the Wigner-Seitz (WS) spheres used in the atomic sphere approximation (ASA) have to be replaced by the exact WS cells, which are non-overlapping and fill up the whole space completely. This is done by the use of a step function $\Theta(\mathbf{r})$ which is one inside the WS polyhedron and zero outside, and is used to truncate the potential outside the cell. All integrals are convoluted with $\Theta(\mathbf{r})$ which is expanded in spherical harmonics:

$$\Theta(\mathbf{r}) = \sum_L \Theta_L(r) Y_L(\mathbf{r}) \quad . \tag{23}$$

The expansion coefficients can be calculated for polyhedra of arbitrary shape[5]. Note that the expansion (Eq. (23)) is converging very slowly. However this is not a real problem for the calculations, since expanding the wave functions in spherical harmonics and restricting the angular momentum expansion to a cut-off $l_{max}$ imposes a natural cut-off of $2l_{max}$ for the charge density and the potential. Therefore in the evaluation of the Coulomb integrals naturally only $\Theta_L$-coefficients up to $4l_{max}$ are required, and this cut-off is also highly accurate for the exchange-correlation terms.

**Force Calculations**

An accurate treatment of the full-potential is crucial for the calculation of forces, since in deriving an expression for the force, the extremal properties of the total energy are used, so that the force formula is no longer variationally invariant. By taking the derivative of the total energy with respect to the coordinate $\mathbf{R}^m$ of atom $m$, the force is given by

$$\mathbf{F}^m = -\frac{\partial E}{\partial \mathbf{R}^m}|_{n(\mathbf{r};\mathbf{R^m})} - \int d\mathbf{r} \frac{\delta E}{\delta n(\mathbf{r})} \frac{\partial n(\mathbf{r};\mathbf{R}^m)}{\partial \mathbf{R}^m} = Z^m \frac{\partial V}{\partial \mathbf{r}}|_{\mathbf{r}=\mathbf{R}^m} \tag{24}$$

The first term, to be evaluated for constant density $n(\mathbf{r};\mathbf{R}^n)$, is the Hellmann-Feynman (HF) force, being given by the electric field $\frac{\partial V}{\partial \mathbf{r}}$ of the electrons on the nuclear charge $Z^m$ of the nucleus. The second term gives corrections due to approximations made in the solution of the Kohn-Sham equations. It vanishes in an exact treatment, since then $\frac{\delta E}{\delta n(\mathbf{r})} = E_F$ is a constant. Within the full-potential KKR formalism, the Kohn-Sham equations for the valence electrons are solved practically exactly, with the only approximation being the $l_{max}$ cut-off. However, the use of the HF-formula, i.e. the first term in Eq. (24), requires also a full-potential treatment of the core electrons. If an atom is shifted, the charge density of the core electrons experiences in a solid a small anisotropic distortion induced by the crystal field, which leads to an important contribution to the force on the nucleus and which unfortunately cannot be described in a spherical-core treatment. This problem can be overcome by making a spherical ansatz for the core density entering in the total energy expression. The force is then calculated as the derivative of the total energy with respect to the nuclear position assuming that the Kohn-Sham equations are solved exactly for the valence electrons only. The resulting expression for the force $\mathbf{F}^m$ on the atom $\mathbf{R}^m$ is given by[6]

$$\mathbf{F}^m = Z^m \frac{\partial V_M(\mathbf{r})}{\partial \mathbf{r}}|_{\mathbf{r}=\mathbf{R}^m} - \int d\mathbf{r} n_c(\mathbf{r}-\mathbf{R}^m) \frac{\partial V(\mathbf{r})}{\partial \mathbf{r}} \tag{25}$$

where $Z^m$ is the nuclear charge and $n_c(\mathbf{r}-\mathbf{R}^m)$ the core charge density of atom $m$. Furthermore $V_M(\mathbf{r})$ is the Madelung potential and $V(\mathbf{r})$ the Kohn-Sham potential. While the first term is the force on the nucleus as given by the Hellmann-Feynman theorem (but without the contribution from the core electrons at atom $\mathbf{R}^m$), the second term represents the force on these core electrons and also includes an exchange-correlation contribution, arising from the exchange between valence and core electrons. Thus basically Eq. (25) gives the force on the ion consisting of the nuclear charge and the core charge of atom $m$. Due to the vector character of the potential derivatives in Eq. (25), only the $l=1$ components of the potentials $V_M(\mathbf{r})$ and $V(\mathbf{r})$ are needed for the force. Since in the present full-potential treatment the coefficients $V_L(r)$ are anyhow calculated during the selfconsistency cycles, the calculation of the force does not require additional efforts. Moreover the $l=1$ components of the potentials are essentially determined by the $l=1$ components of the valence charge density $n(\mathbf{r})$. Therefore one obtains only contributions from the interference of wave functions differing by $\Delta l = \pm 1$, i.e. sp, pd, df, fg, ... interference terms.

**Lattice Relaxations**

In contrast to the simplicity of the force calculation, the description of lattice relaxation effects is rather complicated within the KKR method. The main reason is the site-centered angular momentum expansions used in the Green function. In the case of lattice relaxations one needs an angular momentum expansion around the shifted position, i. e. around a non-lattice site. While in principle the host Green function can be calculated for any interstitial site by introducing a supercell with additional empty positions, this is a cumbersome procedure for the small lattice relaxations occurring for substitutional defects. In this case a transformation formalism, used e.g. in Ref. 6, is more convenient. The structural host Green function is transformed from the unshifted coordinates to the new ones being shifted by $\mathbf{s}^n$

$$\tilde{G}^{nn'}_{LL'}(E) = \sum_{L''L'''} U_{LL''}(\mathbf{s}^n;E) G^{nn'}_{L''L'''}(E) U_{L'L'''}(\mathbf{s}^{n'};E) \tag{26}$$

where

$$U_{L'L}(\mathbf{s};E) = 4\pi \sum_{L''} \imath^{l'+l''-l} C_{LL'L''} j_{l''}(\sqrt{E}s) Y_{l''}(\mathbf{s}) \tag{27}$$

The $\tilde{G}$ is the host Green function but expanded in the shifted coordinate system. An analogous U transformation has to be done for the t-matrix. Finally we must solve the following Dyson equation for the structural Green function to obtain the new Green function for potentials or t-matrices on the shifted sites.

$$\bar{G} = \tilde{G}^0 + \tilde{G}^0[t-\tilde{t}^0]\bar{G} \tag{28}$$

where $\tilde{G}^0$ and $\tilde{t}^0$ are the host Green function and host t-matrix in the angular momentum expansion around the shifted sites (Eq. (26)). Thus, apart from the $U$-transformation, the structure of the Dyson equation is unchanged. While the $U$-transformation Eq. (26) is exact, if the sums over $L''$ and $L'''$ are extended over infinite angular momenta, in practical calculations an $l_{max}$-cut-off is used. As can be seen from Eq. (27), for small $s$ the $U_{LL'}$-matrix couples states with $l-l' = \pm 1$. Thus a relatively high $l_{max}$ has to be chosen and

the error increases with increasing displacements. Typically calculations for substitutional defects with $l_{\max} = 4$ are sufficiently accurate up to displacements of 10 % of the nearest neighbor distance. For larger displacements or interstitial defects the Green function $\tilde{G}^{nn'}_{LL'}$ has to be determined by Brillouin zone integration.

# 4 Impurities in Metals and Semiconductors

## 4.1 Lattice Relaxations around Impurities

Substitutional impurities have in general a different size than the host atoms, which leads to lattice displacements of the neighboring host atoms away from their positions in the ideal lattice. Due to the high coordination number, in metallic systems these relaxations are usually very small, not more than a few percent of the nearest neighbor distance, so that calculations without lattice relaxations give usually quite reasonable results. As an example Figure 1 shows the displacements of the nearest neighbors (NN) around 3d impurities in Cu[6]. The displacements are given in terms of the NN distance. In most cases the Cu lattice is dilated due to the impurities, except for the case of Fe, Co and Ni. The triangles with error bars are the results of EXAFS measurements, which allow a direct determination of the relaxations. The bump in the curve with the maximum at Cr is a magneto-elastic effect. The transition metal impurities Cr, Mn and Fe are magnetic with rather large local moments of 2.9 $\mu_B$ (Cr), 3.4 $\mu_B$ (Mn) and 2.5 $\mu_B$ (Fe). Calculations without spin polarization lead the expected parabolic behavior of the displacements across the 3d-series.

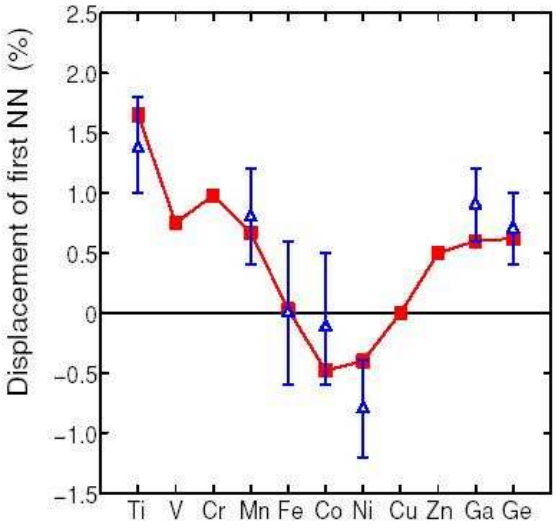


Figure 1. Calculated lattice relaxations around $3d$ and $4sp$ impurities in Cu. The displacements of the nearest neighbor Cu atoms (in percentage of the nearest-neighbor distance) are given. The triangles with error bars refer to EXAFS results[6].

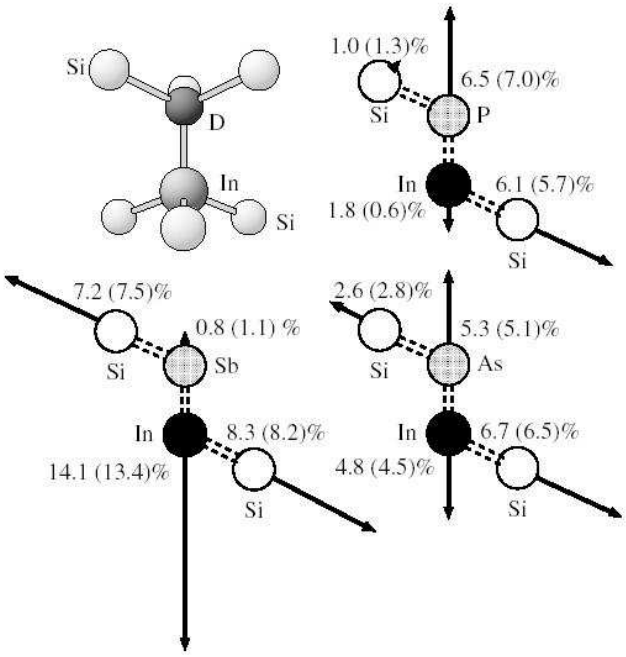


Figure 2. Ground-state configuration of In-donor complexes in Si (InSb, InP, InAs). The numbers denote the relaxations in percentage of the nearest-neighbor distance. The first number refers to KKR calculations, the second one (in brackets) to pseudopotential results[7].

In contrast to metallic alloys lattice relaxations around defects in semiconductors can be much larger, being a result of the more open lattice structure and the lower coordination number of the diamond or zinc blende lattice. Here we discuss the relaxations around acceptor-donor complexes on nearest neighbor sites in Si, such as InSb, InAs and InP pairs in Si. These defects are electrically and magnetically inactive and experimental information about the structure is difficult to obtain. One of the few methods to investigate such defects are perturbed angular correlation (PAC) experiments which measure the electric field gradients. In Figure 2 we present the calculated atomic configurations for In-P, In-Sb, In-As pairs in Si. The full-potential KKR results are compared with the results obtained from pseudopotential calculations. The atomic configurations obtained using both *ab initio* methods are essentially the same, but the KKR can give direct access to properties that are determined by the core electrons, like hyperfine fields or electric field gradients. The electric field gradients (EFG) of the Cd-donor pairs in Si and Ge have been measured. While calculations without lattice relaxations give the wrong trend with respect to the atomic numbers of the donor atoms, the agreement greatly improves, if the relaxed configurations, as e.g. given in Figure 2 for the corresponding In-pairs in Si, are considered[7]. Thus a reliable calculation of the relaxations is decisive for understanding the EFG. (The EFG is basically determined by the second derivative of the electrostatic potential at the nucleus. Thus it has some similarity to the force, which is determined by the first derivative at the nucleus.)

### 4.2 Isomer Shifts and Charge Transfer in Fe Alloys

Isomer shifts of Mössbauer nuclei are directly related to the local charge density $\rho(0)$ at the nuclear position. They therefore provide unique information about charge-density changes upon alloy formation. Unfortunately the changes $\Delta\rho(0)$ are very much smaller than the total charge density $\rho(0)$ at the nucleus, $\Delta\rho(0) \sim 10^{-6}\rho(0)$, so that great numerical precision in needed to calculate isomer shifts. The standard Mössbauer nucleus is Fe. Therefore a large number of Mössbauer data exist for Fe alloys, in particular dilute Fe alloys. Here in addition to the bulk Mössbauer line a satellite is measured arising form the charge perturbation of the Fe nuclei adjacent to the impurities and being shifted from the main line. It is generally believed that these lines give direct information about the charge transfer in these alloys.

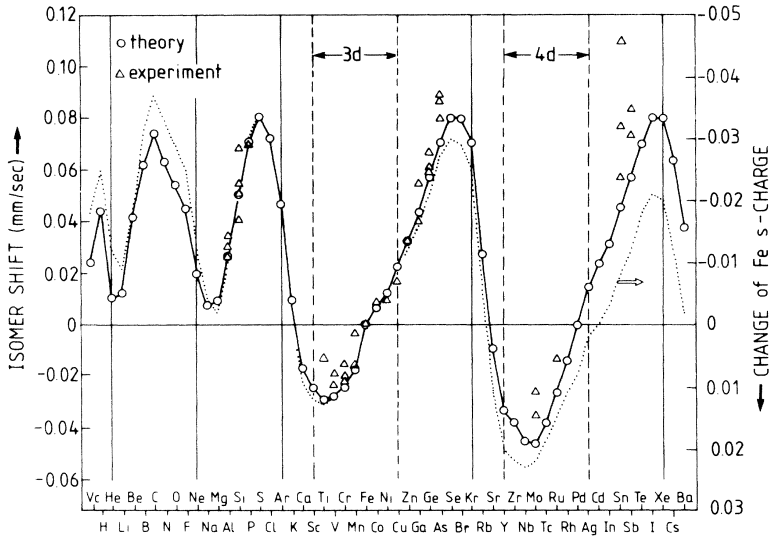


Figure 3. Calculated isomer shift of a nearest neighbor Fe atom as a function of the nuclear charge Z of the impurity (left hand scale). The triangles are experimental values for dilute Fe alloys. The dotted line gives the change $\Delta n_s$ of the number of Fe $s$ electrons and refers to the right-hand scale[8].

Figure 3 shows the calculated isomer-shift values for the NN Fe atom around the impurities and the comparison with the experimental data for these alloys as a function of the nuclear charge $Z$ of the impurity[8]. The triangles refer to experimental data. The general agreement is fairly good and the experimental trends are well reproduced. In general the shifts show a minimum at the beginning of each row of the periodic system and slowly increase to a maximum at the end of the row, dropping sharply to the minimum at the beginning of the next row, etc. However, the periodicity is far from being perfect. For instance, with increasing row number the maxima systematically shift to larger Z values and the minima get more pronounced. We also see systematic deviations between the calculated and experimental values, in particular for the 4d and 5sp impurities. For these oversized impurities lattice relaxations are expected to be significant, which are not included in the

calculations.

Since a negative (positive) isomer shift means that the charge $\rho(0)$ at the NN Fe nucleus has increased (decreased), the behavior seen in Figure 3 follows simple electronegativity arguments that the charge flows from the element with the lower electronegativity to the one with the higher electronegativity. For instance, in the 3d series the charge should flow from the impurity to the NN Fe atoms if the impurity is on the left-hand side of Fe in the periodic table, whereas the charge should flow to the impurity if it is on the right-hand side of Fe. However, this is certainly a too-simplified description, since the isomer shift only measures the change of the charge density $\Delta\rho(0)$ at the Fe nucleus, which moreover is only of s character. No direct information is obtained about $p$- or $d$-electrons. The question therefore arises as to how the changes $\Delta\rho(0)$ are related to the changes of the valence charges, i.e., the changes $\Delta n_s$, $\Delta n_p$, and $\Delta n_d$ of the numbers of $s$, $p$, and $d$ valence electrons of the NN Fe atom.

Indeed the calculations show that the trend of the isomer shifts of the NN Fe atoms is determined by the change of the Fe $s$-valence charge, which is shown by the dotted line in Figure 3. Compared to this the change of the $s$-core charge density at the origin is relatively small and shows no strong systematic trend. Moreover the changes of the $p$- and $d$-charges, which might screen the $s$-wave function and in this way might change the $s$-density at the nucleus, are not significant. In fact, if this would be the case, the trends for the isomer shifts would be very different, since in the $sp$-impurity series the Fe d-charge strongly increases, will the $s$-charge moderately decreases. Thus we see, that for the dilute Fe-alloys, the isomer shift is determined by the change $\Delta n_s$ of the valence $s$-charge[8], which seems to be generally valid in metallic alloys.

## 5 Non-Collinear Configurations of 3d Impurities on Ferromagnetic Surfaces

In this section we consider some recent calculations[9] for non-collinear configurations of 3d-dimers and multimers on the surfaces of ferromagnets. Here the unperturbed surfaces are ferromagnetic with a collinear moment configuration. Thus the Green function $\overset{\circ}{G}$ and $t$-matrix $\overset{\circ}{t}$ of the ideal surface are diagonal is spin-space

$$\overset{\circ}{G}(E) = \left\{ \begin{array}{cc} \overset{\circ}{G}_{\uparrow\uparrow}(E) & 0 \\ 0 & \overset{\circ}{G}_{\downarrow\downarrow}(E) \end{array} \right\} \quad \overset{\circ}{t}(E) = \left\{ \begin{array}{cc} \overset{\circ}{t}_{\uparrow\uparrow} & 0 \\ 0 & \overset{\circ}{t}_{\downarrow\downarrow} \end{array} \right\} \tag{29}$$

while non-collinear states lead to non-diagonal $t$-matrices for the impurity atoms and the surrounding substrate neighbors.

$$t(E) = \left\{ \begin{array}{cc} t_{\uparrow\uparrow} & t_{\uparrow\downarrow} \\ t_{\downarrow\uparrow} & t_{\downarrow\downarrow} \end{array} \right\} \tag{30}$$

The basic approximation with respect to non-collinearity consists of the assumption, that the exchange-correlation potential of each atom $\mathbf{R}^n$ has a unique quantization axis $\mathbf{e}^n$, being common to the whole cell $n$ and determined by the direction of the local moment $\mathbf{M}^n$ in cell $n$. In this local reference frame, the $t$-matrix $t^n$ is diagonal

$$t^n_{loc} = \left\{ \begin{array}{cc} t^n_{\uparrow\uparrow} & 0 \\ 0 & t^n_{\downarrow\downarrow} \end{array} \right\} \tag{31}$$

and the local radial functions $R^n_\ell$ and $H^n_\ell$ are spin dependent as in a collinear calculation. However the Dyson equation describing the multiple scattering events has to be evaluated in a common global frame of reference, as e.g. determined by the magnetization direction of the substrate. The corresponding transformed $t^n$-matrices are given by

$$t^n_{glob}(E) = U_n \, t^n_{loc}(E) \, U^t_n \tag{32}$$

where the rotation matrix $U_n$ of spin space is given by

$$U_n \left( \begin{array}{cc} \cos(\frac{\theta_n}{2}) \, e^{-i\phi_n/2} & -\sin(\frac{\theta_n}{2}) \, e^{-i\phi_n/2} \\ \sin(\frac{\theta_n}{2}) \, e^{i\phi_n/2} & \cos(\frac{\theta_n}{2}) \, e^{i\phi_n/2} \end{array} \right) \tag{33}$$

Here $\theta_n$ and $\phi_n$ are the polar angles defining the direction of the local moment $\mathbf{M}^n$ with respect to the substrate moments.

The basic reason for non-collinear states is "frustration", arising from the competition between ferromagnetic and antiferromagnetic coupling. In addition, also spin-orbit coupling can lead to a non-alignment of the local moments. However this is a very weak effect for transition metals, for which frustration is much more important. We will illustrate this in the following for transition metal dimers on the Ni(001) surface.

Let us start with single 3d adsorbate atoms on Ni(001). The calculations show, that the 3d adatoms have large and stable local moments. The moments of the Co, Fe and Mn adatoms couple ferromagnetically to the substrate moments, while the V and Cr moments prefer an antiferromagnetic coupling to the substrate. The situation of two 3d-adatoms forming a dimer is illustrated in Figure 4. Three kind of dimers are shown: Dimer 1 with the adatoms on nearest neighbor sites, Dimer 2 with the adatoms on second neighbor sites and Dimer 3 on fourth neighbor site. For the Dimer 2 and dimers with larger separation the interaction of the dimer atoms is very small and the configuration is dominated by the interaction with the substrate, meaning that these dimers show the same behavior as the single adatoms, coupling antiferromagnetically to the substrate in the case of V and Cr and ferromagnetically in the case of Mn and Fe, such that both adatoms are parallel aligned to each other. The same is also correct for the NN dimers of Fe or V, where the dimer atom interaction is strongly ferromagnetic (for Fe) or weakly antiferromagnetic (for V). In the case of the Cr and Mn dimers the situation is more complicated, since the interaction of the dimer atoms is strongly antiferromagnetic, favoring an antiferromagnetic pairing of the two moments. However, this is in contradiction to the interaction with the substrate moments, which as explained above, favors a parallel alignment of the impurity moments. Therefore frustration occurs, which can lead to a non-collinear ground state.

The situation is most easily explained, if a model operator in form of the classical Heisenberg model

$$H = -\frac{1}{2} \sum_{i \neq j} J_{ij} \mathbf{e}_i \cdot \mathbf{e}_j \tag{34}$$

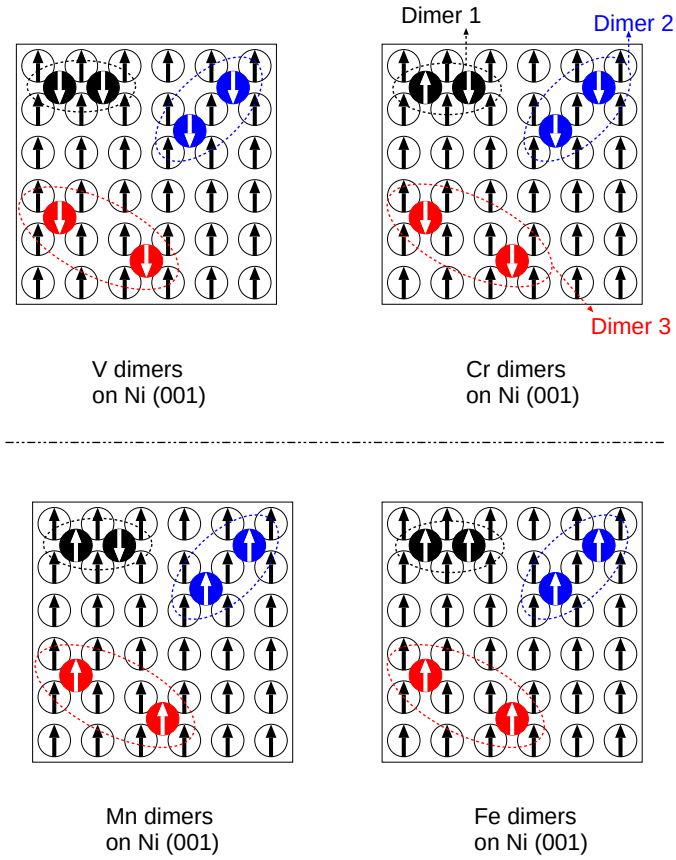


Figure 4. Different geometrical configurations considered for dimers at the surface of Ni(001). Dimer-1–type corresponds to the case where the atoms are first neighboring atoms, dimer-2–type where the atoms are second NN and finally dimer-3–type to fourth NN. The collinear magnetic ground state are also shown for V, Cr, Mn and Fe dimers.

is used. Here $J_{ij}$ is the exchange integral between the atoms $i$ and $j$ and $\mathbf{e}_i$ defines the direction of the local moment $M_i$. By applying this to the interaction of the two adatoms $A = 1, 2$ and their interaction with the Ni moments, which for simplicity are assumed to be fixed, the Hamiltonian is

$$H = -J_{A-A}\cos(\theta_1 - \theta_2) - 4J_{A-Ni}(\cos\theta_1 + \cos\theta_2) \tag{35}$$

where $\theta_1$ and $\theta_2$ are the angles with the respect to the substrate magnetization.

Let us now consider two typical spin configurations, shown in Figure 5(a) and Figure 5(b). Figure 5(a) refers to a collinear configuration, which we call ferrimagnetic, since the two moments, being antiferromagnetically aligned, are not equivalent anymore, resulting in a small, but finite total moment. This configuration is also a selfconsistent solution of the Kohn-Sham equations, if the collinear constraint is removed. This can be

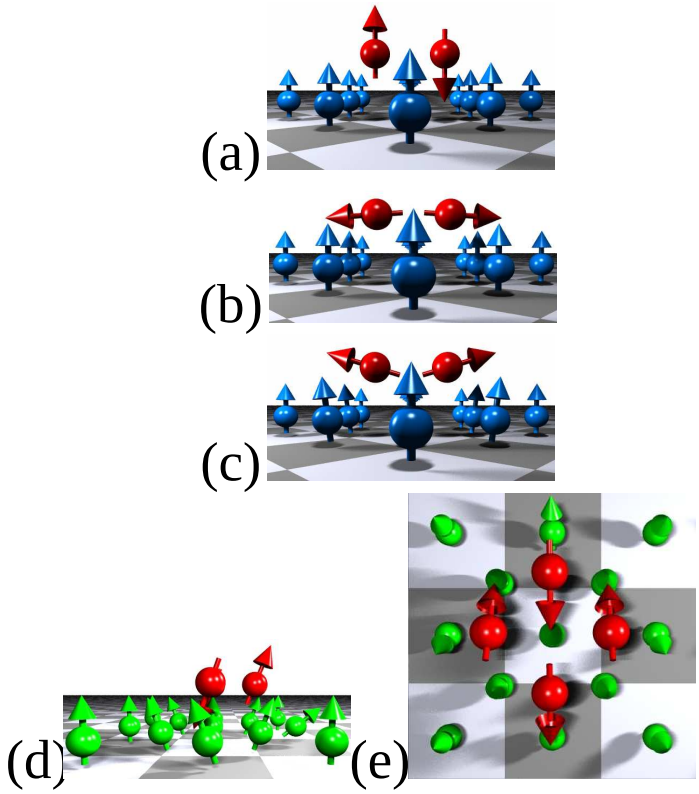


Figure 5. Most stable configurations of Cr and Mn dimer on Ni (in blue) obtained with (a) the collinear KKR method and (b)-(c) the non-collinear KKR method[9]. For Cr(Mn) the rotation angle with respect to the $z$ axis is equal to 94.2°(72.6°) and the collinear(non-collinear) state is the ground state (see text). (d) shows a side view of the stable Cr trimer on the $fcc$ Fe(001) surface (in green), with two Cr atoms pointing down (the second one cannot be seen), one Cr atom pointing up. (e) shows the stable Cr tetramer on the same $fcc$ Fe surface.

understood e.g. from the Heisenberg model Eq. (35), since $\theta_1 = 0$, $\theta_2 = 180^o$ and small variations around these angles change the cos-values in Eq. (35) only in second order, so that the total energy is an extremum. The configuration in Figure 5(b) is non-collinear, but has the same energy as the collinear configuration (a), since in configuration (a) the interaction of the two adatoms with the substrate atoms cancel each other, while in configuration in Figure 5(b) they vanish for both atoms since $\cos\theta_1 = 0 = \cos\theta_2$. However this configuration is not a selfconsistent solution of the non-collinear Kohn-Sham equations, since a small variation $\Delta\theta_1$ and $\Delta\theta_2$ around the values of $90^o$, respectively $270^o$, changes the energy linearly in $\Delta\theta_1$ and $\Delta\theta_2$. Thus there exists a force which tilts the moments slightly towards or away from the surface, depending on the sign of $J_{A-Ni}$. In fact the configuration (b) is the non-collinear solution for a Cr dimer. With a rotation angle of $94^o$, deviating only slightly from $90^o$ (which can hardly be seen in the figure), a small energy is gained due to the antiferromagnetic coupling with the substrate $(J_{Cr-Ni} < 0)$. In contrast to this the configuration in Figure 5(c) is the selfconsistent solution for a Mn-dimer, which prefers a ferromagnetic coupling with the substrate atoms ($J_{Mn-Ni} > 0$). Here the angle

with respect to the z-axis is $73^o$, the deviation from $90^o$ is much larger. The *ab initio* calculation shows, that this is the ground state for the Mn-dimer. However for the Cr dimer the collinear solution of Figure 5(a) is the ground state, which is in contradiction to the Heisenberg model and arises from small changes of the local moments upon rotation, an effect which cannot be described by this model.

In Figure 5(d) and (e) we show two other non-collinear configurations obtained in the *ab initio* calculations, the configurations for compact Cr trimers and Cr tetramers on fcc $Fe_{3ML}$/Cu(001). In this case the exchange interactions are very similar, except that the antiferromagnetic coupling of the Cr adatoms to the Fe substrate atoms is considerably stronger. In both cases the Cr-Cr interaction is strongly antiferromagnetic. For the trimer, it is most important, that the effective interaction with the substrate moments is non-zero in the collinear configuration, but zero in the planar configuration. Thus the (basically) collinear configuration with the outer Cr atoms antiferromagnetically aligned to the surface moments and the central Cr atom ferromagnetically aligned is favored. However an additional small tilting occurs, in particular for the wrongly aligned central Cr atom, which further lowers the energy, so that also this configuration becomes non-collinear.

For the tetramer, the neighboring Cr atoms couple again antiferromagnetically. For the in-plane configuration, similar to the dimer, the effective interaction with the substrate moments vanishes, however slight tiltings of the moments towards the surface lead to an additional energy gain stabilizing the in-plane configuration.

## 6 Quantum Corrals on the Cu(111) Surface

Over the last decades a great deal of experimental and theoretical efforts has been devoted to study electrons in two-dimensional (2D) surface states. Here the (111) surface of the noble metals has served as a model system, exhibiting a surface state in the gap around the $L$-point of the bulk Brillouin zone. For Cu(111) this state shows a parabolic dispersion with a minimum at 0.39 eV below the Fermi level. The corresponding band structure projected on the $\bar{\Gamma} - \bar{M}$ line of the 2D-Brillouin zone is shown in Figure 6. The shaded regions give the regions in $E - \mathbf{k}_{\|}$ space, for which bulk eigenstates (Bloch waves) exist. Surface states can only exist in the white "gap"-regions. Two such states are indicated. Of special interest is the parabolic band with the minimum close to $E_F$, since this state is only partially occupied and gives rise to a two-dimensional metallic behavior, which is of great interest for the following.

In this lecture we are interested in defects and small clusters in the bulk and on surfaces. As is well known, in metallic systems point defects cause long ranged charge oscillations (Friedel oscillations), which are governed by the Fermi surface properties. For defects in the bulk, these Friedel oscillations of the charge perturbation vary for large distances $r$ as $1/r^3$ times an oscillatory function and are in the jellium model proportional to:

$$\delta n(r) \;\sim\; \frac{\cos(2k_F r + \delta)}{r^3} \quad . \tag{36}$$

However in the case of adatoms on surfaces, the charge response decays for long in-plane distances $\rho$ slower than in the bulk and is determined by the surface states. In a free electron model, being well suited for the above surface state for Cu(111), for large distances the charge density is $\rho$ proportional to

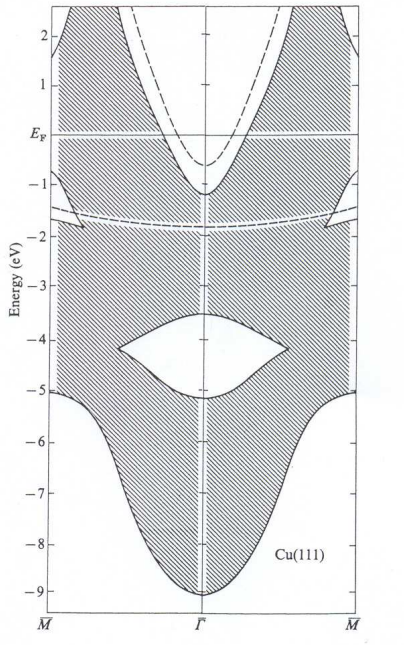


Figure 6. Surface states (dashed curves) and bulk projected bands at a Cu(111) surface according to a six-layer surface band structure calculation[10].

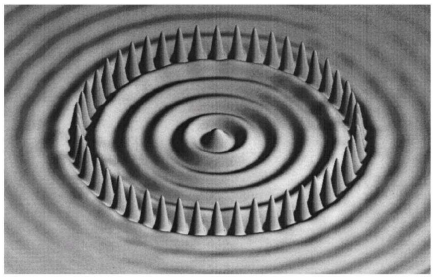

Figure 7. LDOS at the Fermi energy in and around a 142.8 Ångstrøm diameter circular corral of 48 Fe atoms on Cu(111)[12].

$$\delta n(\rho) \sim \frac{\sin(2k_F\rho + \delta)}{\rho^2} \quad . \tag{37}$$

However, since also bulk states exist, which span most of the phase space (see Figure 6), the short range screening of the defect is dominated by these states, while only the long ranged behavior is determined by the surface state, which has a small wave vector $k_F$ leading to long wave length oscillations.

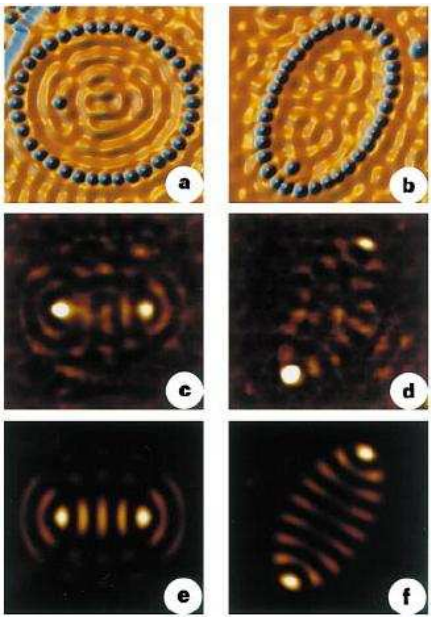


Figure 8. Visualization of the quantum mirage. **a**, **b**, Topographs showing the $e = \frac{1}{2}$ (**a**) and $e = 0.786$ (**b**) ellipse each with a Co atom at the left focus. **c**, **d**, associated $\frac{dI}{dV}$ difference map showing the Kondo effect projected to the empty right focus, resulting in a Co atom mirage. **e** and **f**, Calculated eigenmodes at $E_F$ (magnitude of the wave function is plotted)[13].

Many authors have observed such long ranged oscillations around adatoms, small clusters and steps on the Cu(111) surface in STM experiments. Most prominent among these is the work of Eigler et al.[12]. By atomic manipulations they were able to construct a corral of Fe atoms on the (111) Cu surface, and have shown that the surface states in the corral are more or less localized and form a discrete spectrum of resonant states. As an illustration of these we show in Figure 7 the result of KKR calculations of Crampin *et al.*[11] for a circular corral of 48 Fe atoms on the Cu(111) surface. Shown are the local density of states at the Fermi energy and 5 Ångstrøm above the surface. Within the corral one sees a quantum well state with five maxima, corresponding to a localized state being more or less completely confined to the corral. Outside one sees oscillations arising from scattered surface state electrons at the corral, which decay with distance.

Let us shortly discuss the reason for the strong scattering of the surface state electrons at the Fe atoms. Basically in the vacuum region the full-potential of Fe acts as a scattering center for the surface wave, being much stronger than the scattering at an Fe impurity in the bulk, where only the change of the Fe potential with respect to the host potential is effective. Moreover the wave vector $k_F$ is relatively small, such that the wave length is considerably larger than the spacing between the Fe atoms. Therefore the surface wave does not "see" the corrugation of the Fe ring and is strongly reflected as in cylindrical well. In fact the sequence of resonances can be well described by such a quantum well model, as has been shown recently[14]. The most fascinating corral experiments are the observation

of atomic mirages in an elliptical quantum well[13]. An ellipse has the well known property that all classical waves emanating from one of the two focus points in every direction are reflected from the ellipse wall and focused in the second point, where these waves add up coherently since each such partial wave has the same path length and therefore the same phase shift. This is illustrated in Figure 8 taken from the letter of Manoharan *et al.*[13]. Figure 8(a) and (b) show the STM topography for two ellipses with different eccentricities, each including one Co atom at the left focus point. Figure 8(c) and (d) show the $\frac{dI}{dV}$ difference maps, *i.e.* the change of the STM intensity map with respect to a small bias voltage V, which corresponds in the calculations to the local density of states in the vacuum region at the height of the STM tip. We see clearly two intensity spots, the real Co atom at the left focus and its image at the right focus. Thus in the empty focus we see the same accumulation of charge in the surface state as around the Co atom; therefore the image is called a quantum mirage. In fact the Co atom is a Kondo impurity and a strong and sharp Kondo peak appears only in a very small energy region of about 10 meV around the Fermi level. Moreover the large mirage only appears, if one of the quantum well states falls into this energy region. Figure 8(e) and (f) show the calculated localized eigenstate observed in the experiment. The calculated local density of states compares very well with the $\frac{dI}{dV}$ curves shown in Figure 8(c) and (d). Thus several conditions have to be satisfied for the Co mirage to appear: (i) the Co-atom has to sit in a focus point; if it sits at another position away from the focus point, no image appears, (ii) the bias voltage has to be such, that it coincides with an eigenstate of the ellipsoidal corral having maxima at the focus points, (iii) finally the image is particularly intense, if the eigenvalue coincides with the Kondo resonance.

## 7 Conclusions

In the lecture of Mavropoulos and in this one you have seen that the KKR Green function method is an excellent tool for ground state calculations, which is particularly well suited for nanostructures like surfaces, multilayers, impurities and clusters on surfaces etc. However, compared to other methods it is somewhat complicated and demanding, in particular when lattice relaxations are needed. Its basic advantage is the availability of the Green function, which allows to do more than just ground state calculations. One can do linear response with respect to an electric or magnetic field and can treat quantum transport based on Kubo-Greenwood or Landauer formalism. Another example are calculations for disordered alloys based on the coherent potential approximation (KKR-CPA). Also for the problem of excited states the availability of the Green function is an important plus.

## References


1. T. H. Dupree, Ann. Phys. (N. Y.), **15**, 63 (1961); J. L. Beeby, Proc. Roy. Soc. London Ser. A**302**, 113 (1967); G. J. Morgan, Proc. Phys. Soc. **89**, 365 (1966).
2. W. Kohn and N. Rostoker, Phys. Rev. **94**, 1111 (1954).
3. R. Zeller, J. Phys. C **20**, 2347 (1987).
4. B. Drittler, Dissertation, Rheinisch-Westfälische Technische Hochschule Aachen (1991).

5. N. Stefanou and R. Zeller, J. Phys.: Condens. Matter **3**, 7599 (1991).
6. N. Papanikolaou, R. Zeller, P. H. Dederichs, and N. Stefanou, Phys. Rev. B **55**, 4157 (1997).
7. A. Settels, T. Korhonen, N. Papanikolaou, R. Zeller, and P. H. Dederichs, Phys. Rev. Lett. **83**, 4369 (1999).
8. H. Akai, S. Blügel, R. Zeller, and P. H. Dederichs, Phys. Rev. Lett. **56**, 2407 (1986).
9. S. Lounis, Ph. Mavropoulos, P. H. Dederichs, and S. Blügel, Phys. Rev. B **72**, 224437 (2205)
10. A. Euceda, D. M. Bylander, and L. Kleinman, Phys. Rev. B **28**, 528 (1983).
11. S. Crampin and O. R. Bryant, Phys. Rev. B **54**, 17367 (1996).
12. M. F. Crommie, C. P. Lutz, and D. M. Eigler, Science **262**, 218 (1993).
13. H. C. Manoharan, C. P. Lutz, and D. M. Eigler, Nature **403**, 512 (2000).
14. B. Lazarovits, B. Újfalussy, L. Szunyogh, B. L. Györffy and P. Weinberger, J. Phys.: Condens. Matter **17** S1037 (2005).